ACS APPLIED NANO MATERIALS

www.acsanm.org Article

Luminescent Zero-Dimensional Hybrid Lead Thiohalide Nanostructures for High Quantum Yield and Broadband Excitation

Nicolay N. Golovnev,* Aleksandr S. Aleksandrovsky,* Marina A. Gerasimova, Felix N. Tomilin, Vladimir A. Mironov, Anastasia V. Demina, Zhiguo Xia, and Maxim S. Molokeev*

Cite This: *ACS Appl. Nano Mater.* 2021, 4, 3654–3663 Read Online

ACCESS | Metrics & More | Article Recommendations | Supporting Information

ABSTRACT: Luminescent *trans*-[$Pb(DMTU\text{-}S)_4Cl_2$] (DMTU: *N,N′*-dimethylthiourea) was designed and prepared via either mechanochemical or solvothermal methods, and the structures of DMTU and *trans*-[$Pb(DMTU\text{-}S)_4Cl_2$] have been resolved using X-ray single-crystal diffraction. Upon excitation over broadband covering the range from 450 to 250 nm, *trans*-[$Pb(DMTU\text{-}S)_4Cl_2$] shows yellow-green emission peaking at 549 nm with a spectral width of 110 nm, which is assigned to the triplet−singlet transition of Pb^{2+} ions within distorted heterogeneous S_4Cl_2 octahedra. The broadband excitation comprised singlet−singlet transitions of Pb^{2+} ions and energy transfer from orbitals involving those of organic ligands. Simultaneous analysis of the luminescent bandwidth and Stokes shift gives for Pb^{2+} ions in S_4Cl_2 octahedra the value of the Huang−Rhys parameter $S = 4.25$ and the energy of phonon involved in the formation of the luminescence spectrum of the order of 90 meV. Quantum yield as high as 91% is detected for excitation at 365 nm. This high quantum yield indicates the absence of noticeable concentration quenching at an average distance of 9.4 Å between the Pb^{2+} ions within the structure of *trans*-[$Pb(DMTU)_4Cl_2$]. The weak spin−orbit intersystem crossing is deduced from a high photoluminescence quantum yield (PLQY) value. Time dependent-density functional theory (TD-DFT) calculations of the nanocluster indicate the red shift of absorption bands in $Pb(DMTU)_4Cl_2$ with respect to parent DMTU. The high-performance photoluminescence and stability demonstrated promising applications in photonics.

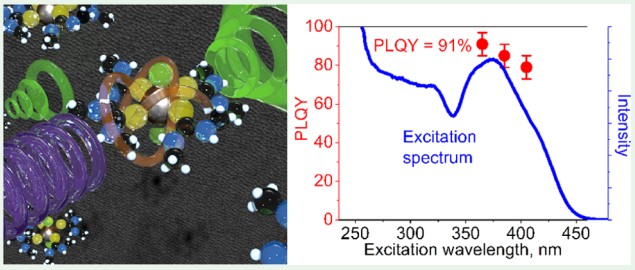

KEYWORDS: *zero-dimensional hybrid metal halide, luminescence, quantum yield, mechanochemical synthesis, X-ray diffraction, dimethylthiourea*

INTRODUCTION

The luminescence of metal−organic frameworks is extensively investigated for several decades. It involves at least seven different mechanisms, including main ones such as organic ligand-centered luminescence and metal-centered ones.[1] More recently, 0D organic−inorganic hybrid metal halides attracted the attention of researchers.[2−8] A comparative study of different luminescent materials based on s^2[2] ions in both organic and inorganic matrices is recently published.[9−12] The photoluminescence quantum yield or PLQY up to 100% was obtained from a variety of 0D hybrid metal halides (see, e.g.,[3]). Both the absorption of exciting radiation and the luminescence in these nanostructured materials are mainly centered at the molecular orbitals contributing by electronic states of metal ions, while the role of organic ligands is, to the first approximation, solicited to the formation of a controllable environment of the ns^2[2] metal ions. However, more detailedly, the properties of organic ligands may influence the properties of metallic luminescence centers within the metal−organic molecule.[13] Employing the energy transfer processes between organic ligands and the metal ions may extend the requirements to the wavelengths of exciting radiation. On the other hand, the formation of organic−inorganic hybrid metal halides may strongly affect the optical properties of organic ligands, e.g., to modify the energy level system of the ligand and to produce an additional absorption of exciting radiation.

Recently, one more role of organic ligands was pointed out, namely, it was shown that the introduction of organic ligands with different geometries allows controlling the distance between manganese ions in the structure of metal−organic phosphor,[14,15] and when large enough distance is attained, the concentration quenching is suppressed, while PLQYs close to 100% become attainable. For other metal ions, including, e.g., lead, no data on the role of ligand geometry in the nanostructure on PLQY are available up to date.

In the current work, the heterogeneous local environment of Pb composed of chlorine and sulfur was chosen to be

Received: January 18, 2021
Accepted: March 10, 2021
Published: March 19, 2021

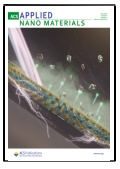

https://doi.org/10.1021/acsanm.1c00162
ACS Appl. Nano Mater. 2021, 4, 3654–3663

Table 1. Crystal Structure Parameters of DMTU (1) and *trans*-[Pb(DMTU)$_4$Cl$_2$] (2)

compound	DMTU (**1**)	*trans*-[Pb(DMTU)$_4$Cl$_2$] (**2**)
chemical formula	$C_3H_8N_2S$	$C_{12}H_{32}Cl_2N_8PbS_4$
molecular weight	104.17	694.78
temperature (K)	296	296
crystal size, mm	0.5 × 0.4 × 0.3	0.3 × 0.2 × 0.1
space group, Z	$P2_1/n$, 16	$P2_1/n$, 2
a (Å)	13.2614 (4)	11.0612 (9)
b (Å)	12.3000 (4)	10.6615 (9)
c (Å)	13.8767 (4)	11.2502 (10)
β (deg)	92.1529 (8)	91.644 (2)
V (Å^3)	2261.90 (12)	1326.2 (2)
ρ_{calc} (g/cm^3)	1.224	1.740
μ (mm^{-1})	0.432	6.892
reflections measured	42625	26769
reflections independent	10030	6396
reflections with $F > 4\sigma(F)$	5636	4218
$2\theta_{max}$ (deg)	70.23	72.58
h, k, l - limits	$-21 \le h \le 21$;	$-18 \le h \le 18$;
	$-19 \le k \le 19$;	$-17 \le k \le 17$;
	$-22 \le l \le 22$	$-18 \le l \le 18$
R_{int}	0.0846	0.0503
	Refinement Results	
The weighed refinement of F^2	$w = 1/[\sigma^2(F_o^2) + (0.148P)^2 + 4.72P]$, where $P = \max(F_o^2 + 2F_c^2)/3$	$w = 1/[\sigma^2(F_o^2) + (0.066P)^2 + 0.493P]$, where $P = \max(F_o^2 + 2F_c^2)/3$
number of refinement parameters	217	124
$R1$ $[F_o > 4\sigma(F_o)]$	0.1353	0.0437
$wR2$	0.3562	0.1118
Goof	1.066	1.029
$\Delta\rho_{max}$ (e/Å^3)	1.99	3.05
$\Delta\rho_{min}$ (e/Å^3)	−0.87	−1.45
$(\Delta/\sigma)_{max}$	<0.001	<0.001
extinction coefficient (SHELXL 2014/7)	none	none

constructed. *N*,*N*′-Dimethylthiourea was taken as a sulfur(-2)-containing ligand. The interaction of thiourea (TU) and its derivatives with metal ions has been the subject of several investigations because of the relevance of their binding sites to those in living systems.[16−23] Thiourea derivatives may coordinate to a metal ion with a variety of coordination modes, and they may exist in syn−syn, syn−anti, and anti−anti conformations.[24] They are widely used in crystal engineering as tectons because of the reliability of the hydrogen bonding patterns that they define.[25,26] Thiourea forms noncentrosymmetric complexes when combined with inorganic salts resulting in enhanced NLO activity.[27−31] The photoluminescence (PL) spectra showed that emission is in the blue region for some synthesized crystals of the thiourea metal complexes with a little Stokes shift.[28−31] Alternatively, the red-colored PL emission with single peak maxima centered at 607 nm in the K(TU)Cl crystal[32] and two emission bands at 358 and 547 nm in $Zn(TU)_2(CH_3COO)_2$[27] were detected. However, the papers[27−32] do not report PLQY and do not discuss the mechanisms of emission. Another coordination polymer $[(CuCN)_2(TU)]_n$ excited by UV radiation displayed two emission bands at 398 and 465 nm with PLQY <1%.[31] The five compounds $[(CuCN)_5(MTU)_3]_n$, $[(CuCN)_3(MTU)_2]_n$ {MTU = *N*-methylthiourea}, $[CuCN(PTU)]_n$ {PTU = *N*-phenylthiourea}, $[CuCN(DPTU)]_n$ {DPTU = *N*,*N*′-diphenylthiourea}, and $[(CuCN)_3(FPTU)_2]_n$ {FPTU = 2,4-difluorophenylthiourea} showed emission quantum yield in excellent values ranging from 3.0 to 20%, with significant Stokes shifts.[33] Thiourea derivatives are used as ancillary ligands, for instance, in luminescent complexes with Pt(II)[34] and Ru(II).[35] The coordination chemistry of thiourea derivatives with p-block elements is less well studied than that of transition metals and, therefore, this could be a matter of research interest. According to our knowledge, the studies of the luminescence of mixed thiourea-halide complexes of Pb(II) are absent. At the same time, the singlet- and triplet-bound excitons, as well as emission from defects, were observed at low temperatures, for instance, in $PbCl_2$[36] and $PbBr_2$.[37] To obtain a luminescent compound with emission in the visible region, we combined $PbCl_2$ with *N*,*N*′-dimethylthiourea (DMTU).[38,39]

The new luminescent nanostructured complex that is under study in the present work has been achieved by directly grinding $PbCl_2$ together with *N*,*N*′-dimethylthiourea, as well as by the solvothermal method. This metal−organic compound exhibits broadband luminescence at room temperature (RT) upon excitation by violet and UV radiation with a significant emission quantum yield close to 100%.

EXPERIMENTAL SECTION

Synthesis of DMTU (1). $PbCl_2$ (Acros) were purchased and used without further purifications. *N*,*N*′-Dimethylthiourea (Aldrich) formed supersaturated solutions in water and 95% ethanol, which was stable for several weeks. Its recrystallization was carried out by the evaporation of 2 mL of water−ethanol (1:1 volumes) solution containing 2 g of DMTU to a volume of 0.5 mL at room temperature, followed by the seeding of a small crystalline reactive DMTU. Single crystals of DMTU

https://doi.org/10.1021/acsanm.1c00162
ACS Appl. Nano Mater. 2021, 4, 3654−3663

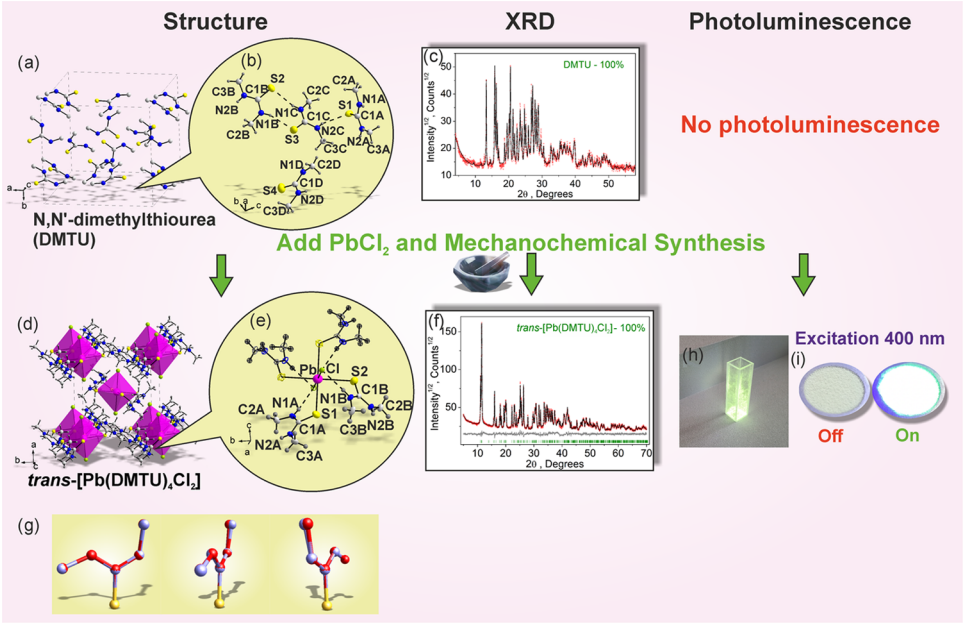

Figure 1. Crystal structure of DMTU (a), all hydrogen atoms were deleted for clarity. The crystal structure of *trans*-$[Pb(DMTU)_4Cl_2]$ (d). The atoms in the asymmetric part of the unit cells DMTU (b) and *trans*-$[Pb(DMTU)_4Cl_2]$ (e) are labeled, symmetry equivalent atoms are represented as empty ellipsoids, and the hydrogen bonds are presented as dashed lines. The thermal ellipsoids are drawn at the 50% probability level. Difference X-ray powder patterns of DMTU (**1**) (c) and *trans*-$[Pb(DMTU)_4Cl_2]$ (**2**) (f). Three different orientations of two imposed average DMTU molecules obtained from structures: DMTU (**1**), a red-colored molecule of DMTU; *trans*-$[Pb(DMTU)_4Cl_2]$ (**2**), a blue-colored molecule of DMTU (g). Photoluminescence of *trans*-$[Pb(DMTU)_4Cl_2]$ under 400 nm excitation: square quartz sample holder (h); a silicic round flat sample holder used for X-ray measurements (i).

(**1**) suitable for X-ray diffraction were selected from the total mass of the precipitate formed.

Synthesis of *trans*-[Pb(DMTU)$_4$Cl$_2$] (2). The compound *trans*-$[Pb(DMTU)_4Cl_2]$ (**2**) was obtained employing both solvothermal and solvent-free (mechanochemistry) methods. The latter is a reliable alternative with several advantages inherent to the higher reaction yield achieved and to the more environmentally friendly approach. The samples of **2** were obtained via kneading (Figure S1), i.e., grinding with a small quantity (0.2−2 mL) of water and 95% ethanol. The hydrothermal technique was also successfully applied. The microcrystals were obtained from mechanochemistry by mixing a stoichiometric amount of the reagents using agate mortar and pestle. The $PbCl_2$ is only sparingly soluble in water; therefore, its solubility was increased due to complexation ($PbCl_2(s) + nCl^- \leftrightarrow PbCl_{n+2}^{n-}$, n = 1,2)[36] by the additional introduction of chloride ions in the form of alkali metal chlorides (Li, Na, K, Cs) and ammonium. To obtain **2** by crystallization from water, a large excess of DMTU was required since Pb(II) ions form unstable complexes with thiourea and its alkyl derivatives.[33] Below, we used three methods leading to single-phase polycrystalline powders (Figure S1) and single crystals, which turned out to be air-stable.

Quantitative white powdered *trans*-$[Pb(DMTU)_4Cl_2]$ was obtained via kneading (500 μL of 95% ethanol) $PbCl_2$ (50.0 mg) and DMTU (74.9 mg) in a stoichiometric ratio 1:4 at room temperature for 30 min with a mortar and pestle.

Polycrystals *trans*-$[Pb(DMTU)_4Cl_2]$ (Figure S1) were also obtained by crystallization from an aqueous solution, 0.050 g (0.18 mmol) of $PbCl_2$ was added to 2 mL of 0.4 M HCl, then the mixture was kept at 90 °C for 5 min. Then, 0.50 mL of a solution containing 0.40 g (3.84 mmol) of *N*,*N*′-dimethylthiourea was added to the hot solution with a small amount of insoluble $PbCl_2$. Pale yellow crystals were formed from the resulting light yellow solution by slowly cooling, which were finally filtered after 3 days, yielding (**2**) 0.073 g or 58% (relative to $PbCl_2$). The powder appeared to be very pure.

Single crystals *trans*-$[Pb(DMTU)_4Cl_2]$ were obtained by reacting *N*,*N*′-dimethylthiourea and $PbCl_2$ in a 95% ethanol solution. The 0.40 g (3.84 mmol) of *N*,*N*′-dimethylthiourea was dissolved in 2 mL of C_2H_5OH, then 0.050 g (0.18 mmol) of $PbCl_2$ was added and heated until it was completely dissolved, after which the solution was slowly cooled. After 30−40 min, the formation of a small number of light yellow crystals of (**2**), as well as colorless $PbCl_2$ crystals, was observed. After a day, the precipitate was filtered off and single crystals (**2**) were manually selected from the total mass of the precipitate.

Characterization. The intensities from single-crystal DTMU (**1**) and *trans*-$[Pb(DMTU)_4Cl_2]$ (**2**) were collected at 296 K using the SMART APEX II X-ray single-crystal diffractometer (Bruker AXS, analytical equipment of Krasnoyarsk Center of collective use of SB RAS) equipped with a CCD-detector Photon2, graphite monochromator, and Mo Kα radiation source. The orientation matrix and cell parameters were defined and refined for a set of 42625 and 26769 reflections for (**1**) and (**2**), respectively. Both unit cells correspond to monoclinic symmetry. Space group $P2_1/n$ was determined from the statistical analysis of the intensities of all of the reflections. The absorption corrections were applied using the SADABS program. The structure was solved by the direct methods using the SHELXS package and refined by the anisotropic approach for nonhydrogen atoms using the SHELXL program.[40] All of the hydrogen atoms of the DMTU ligand were positioned geometrically as riding on their parent atoms with d(C−H) = 0.97 Å for the C−H bonds and d(N−H) = 0.89 Å for all other N−H bonds and $U_{iso}(H) = 1.2U_{eq}(C,N)$. The structural tests for the presence of missing symmetry elements and possible voids were produced using the PLATON program.[41] The main crystal data are shown in Table 1. The crystallographic data were deposited in the Cambridge Crystallographic Data Center (CCDC # 2043053−2043054). The data can be downloaded from the site (www.ccdc.cam.ac.uk/data_request/cif). The main bond lengths are shown in Table S1. The DIAMOND program is used for the crystal structure plotting (Figure 1).[42]

Powder X-ray diffraction data of (**1**) and (**2**) were obtained using a D8 ADVANCE diffractometer (Bruker, analytical equipment of Krasnoyarsk Center of collective use of SB RAS) equipped by a VANTEC detector with a Ni filter. The measurements were made using Cu Kα radiation. The structural parameters defined by single-crystal analysis were used as a basic in powder pattern Rietveld refinement. The

https://doi.org/10.1021/acsanm.1c00162
ACS Appl. Nano Mater. 2021, 4, 3654−3663

refinement was produced using the TOPAS 4.2 program.[43] Low *R*-factors and good refinement results shown in Figure 1c,f indicate the crystal structures of the powder samples to be the representative one of the (**1**) and (**2**) bulk structures.

Spectroscopic Measurements. The absorption spectra of *trans*-[$Pb(DMTU)_4Cl_2$] particles deposited on a quartz substrate were recorded using a spectrophotometer Lambda 35 (PerkinElmer). To do this measurement, a small amount of **2** was deposited at the surface of the quartz substrate.

A spectrofluorometer Fluorolog 3-22 (Horiba Jobin Yvon) was used to measure the photoluminescence (PL) spectra of *trans*-[$Pb(DMTU)_4Cl_2$] powder and particles deposited on a quartz substrate as well as the decays on the microsecond time scale. The PL spectra were obtained under different excitation wavelengths of 250−450 nm. The decays of PL were registered at the wavelength of the spectral maximum of 549 nm with a time interval of 1 μs. The PL spectra were corrected to the following distorting factors: spectral sensitivity of PMT, different intensities of excitation, and the background. All spectral measurements were performed at room temperature using the front face geometry.

The photoluminescence quantum yield (PLQY) was measured using the integrating sphere RTC-060-SF (Newport), spectrometer with fiber-optic input Maya2000 (Ocean Optics), and three LEDs: L365A, L385A, and L405A (Ocean Optics).

COMPUTATIONAL METHODOLOGY

All calculations for crystal structures were performed within the linear combination of the atomic orbital approach, as implemented in the CRYSTAL17 package.[44] The initial atomic coordinates for finding the equilibrium crystal structure were obtained from experimental XRD data. The B3LYP[45] functional has been used for all calculations. In the hybrid functional calculations, the Kohn−Sham orbitals are expanded in Gaussian-type orbitals, as implemented in the CRYSTAL17 code with the basis sets H: H_pob_DZVP_rev2,[46,47] C: C_pob_DZVP_rev2,[46] N: N_pob_DZVP_rev2,[46] S: S_pob_DZVP_rev2,[46] Cl: Cl_pob_DZVP_rev2,[46] and Pb: Pb_ECP60MDF_doll_2011.[48,49] Cut-off limits in the evaluation of Coulomb and exchange series appearing in the self-consistent field (SCF) equation for periodic systems were set to 10^{-7} for Coulomb overlap tolerance, 10^{-7} for Coulomb penetration tolerance, 10^{-7} for exchange overlap tolerance, 10^{-7} for exchange pseudo-overlap in the direct space, and 10^{-14} for exchange pseudo-overlap in the reciprocal space. The condition for the SCF convergence was set to 10^{-6} a.u. on the total energy difference between two subsequent cycles.[50] The gradients with respect to atomic coordinates are evaluated analytically. The equilibrium structure is determined using a quasi-Newton algorithm with a Broyden−Fletcher−Goldfarb−Shanno Hessian updating scheme.[51] The *trans*-[$Pb(DMTU\text{-}S)_4Cl_2$] crystal structure with 30 irreducible atoms in the conventional cell was optimized in $P2_1/c$ symmetry (Figure S2). These calculations are in good agreement with experiment (experiment: a = 11.06120, b = 10.66150, c = 15.54920, β = 133.7°; calculation: a = 11.28762, b = 10.86574, c = 15.72438, β = 134.0°; more details in the Supporting Information).

The model for the absorption spectra simulation was initially the cluster containing one lead atom, two chlorine atoms, and four DMTU molecules connected with lead. Coordinates of atoms within the cluster used for the calculation were derived from CRYSTAL17 calculations. In the course of optimization, the instability of the primary cluster was revealed, and for the stabilization of chlorine atoms, four additional DMTU molecules were added that were connected to chlorine atoms by hydrogen bonds (Table S2). The equilibrium structure was found using hybrid density functional theory (B3LYP) using the GAMESS package with the def2-SVP basis set. These calculations were performed either for dielectric permittivity of ambience ε = 1 for the $(DMTU)_8PbCl_2$ cluster and in water solution (ε = 78.39) using solvation model based on density (SMD) for describing solvent effects for the DMTU molecule.[52] Water ambience was assumed for DMTU since the corresponding absorption spectra were recorded in water solution. The absorption spectra have been predicted using a rigorous time-dependent hybrid DFT scheme (TD/B3LYP/def2-SVP) implemented in the GAMESS package.

RESULTS AND DISCUSSION

Crystal Structure of DMTU. The asymmetric part of the (**1**) unit cell contains four molecules of $C_3H_8N_2S$ (Figure 1b), and the total unit cell contains 16 molecules of DMTU (Figure 1a). Bond lengths d(S−C1), d(N1−C1), d(N1−C2), d(N2−C1), and d(N2−C3) of three independent molecules labeled "A", "B", and "C" are in the narrow ranges of 1.709(4)−1.721(6), 1.317(6)−1.344(6), 1.433(6)−1.459(7), 1.306(5)−1.330(6), and 1.415(8)−1.464(5) Å, respectively (Table S1). However, the last molecule labeled "D" has a noticeable difference from these values (Table S1). The probable geometry of this molecule was obtained with low precision due to the high thermal oscillation of this molecule. During refinement, it was found that the thermal parameters of atoms in molecule D were high; therefore, it was suggested to apply soft constraints on bond lengths and thermal parameters of this molecule. The molecules of DMTU are *syn*−*anti* conformations, which is in good agreement with the fact that *N*,*N*′-dialkylthioureas are present predominantly in the *syn*−*anti* conformation.[24]

Crystal structure (**1**) is stabilized by eight N−H···S hydrogen bonds (Table S2), which joint the molecules $C_3H_8N_2S$ with each other forming a 3D net. Each DMTU molecule has three hydrogen bonds with the closest DMTU molecules, and the main fragment of the hydrogen-bond pattern is presented in the figure (Figure S4).

Crystal Structure of *trans*-[$Pb(DMTU\text{-}S)_4Cl_2$]. The asymmetric part of the (**2**) unit cell contains two molecules of $C_3H_8N_2S$, a half Pb^{2+} ion, and one Cl^- ion (Figure 1e). The Pb^{2+} ion is coordinated by two Cl^- ions and four DMTU through S atoms forming octahedron (Figure 1d). This octahedron is almost ideal because the bond length d(Pb−Cl) is in the very narrow range of 2.9612(11)−2.9667(13) Å and d(Pb−S) is close to the values −2.9798(11) Å (Table S1). The distortion index of a polyhedron was calculated using the equation described in the manuscript,[53] and it has a really small value, D = 0.00235. Bond lengths d(S−C1), d(N1−C1), d(N1−C2), d(N2−C1), and d(N2−C3) of two independent molecules labeled "A" and "B" are in the narrow ranges of 1.701(4)−1.711(4), 1.331(5)−1.331(5), 1.440(6)−1.443(6), 1.322(4)−1.350(5), and 1.447(5)−1.444(6) Å, respectively (Table S1). These values are close to relevant bond lengths of DMTU in (**1**) compound, and DMTU molecules in (**1**) and (**2**) are very similar. The C−S bond length is characteristic of a double bond (typical bond lengths 1.69 Å for C═S bonds). The average N1−C1/N2−C1 bond length is shorter than the normal C_{sp3}−N_{sp2} bond length (1.47 Å), indicating a partial double bond character, whereas the N1−C2/N2−C3 bonds are typical single C−N bonds. To visualize the similarity, it was decided to calculate the average DMTU molecule using A, B, and C in (**1**) (Figure 1g, the red-colored molecule) and average DMTU molecule using A and B in (**2**) (Figure 1g, the blue-colored molecule). After that,

https://doi.org/10.1021/acsanm.1c00162
ACS Appl. Nano Mater. 2021, 4, 3654−3663

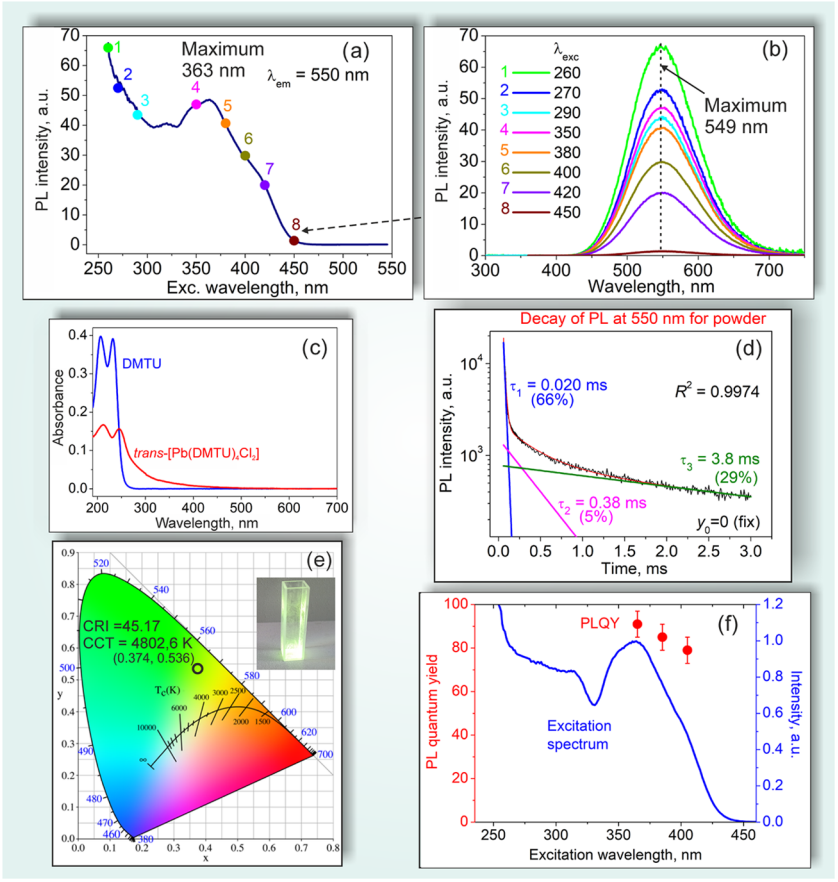

Figure 2. Optical properties of *trans*-$[Pb(DMTU)_4Cl_2]$. The excitation spectrum (a) and PL spectra obtained at different excitations in the range of 250−450 nm labeled 1−9 (b). The values of PL spectra maxima (1−9) are imposed onto the excitation spectrum as circles and have very good fitting (a). Absorption spectrum of *trans*-$[Pb(DMTU)_4Cl_2]$ particles deposited at the surface of the quartz substrate (red) and DMTU in water (blue) (c). The decay of photoluminescence observed at λ_{em} = 550 nm, which can be fitted by three exponents: two (0.020 ms and 3.8 ms decay times) with a significant contribution (66% and 29%, respectively) and one (0.38 ms) with a small contribution (5%) (d). CIE coordinates, CCT, and CRI values obtained from the PL spectrum at λ_{ex} = 350 nm excitation (e). The excitation spectrum and dependence of photoluminescence quantum yield (PLQY) per different excitation wavelength (f).

these molecules were imposed one on another and S atoms were coincided. It was proved that the geometries of molecules are almost the same; the main difference is associated with a small deviation of one terminal CH_3 group (Figure 1g). The molecules of DMTU are in the *syn*−*anti* conformation.

There are two intramolecular and two intermolecular N−H···Cl hydrogen bonds in the structure (Table S2), which forms a 3D net (Figure S4). Each *trans*-$[Pb(DMTU)_4Cl_2]$ cluster is coordinated by eight closest similar clusters (Figure 1d) and linked with them by hydrogen bonds only (Figure S4). Such coordination is similar to the open body-centered-cubic-type structure (bcc), assuming *trans*-$[Pb(DMTU)_4Cl_2]$ clusters as elemental units (Figure 1d). It should be noted that each Cl^- ion is involved in all four N−H···Cl hydrogen bonds: two intramolecular and two intermolecular (Figure S4).

Absorption and Photoluminescence Properties of DMTU and *trans*-$[Pb(DMTU)_4Cl_2]$. The absorption spectrum of DMTU dissolved in water is presented in Figure 2c (blue line). Two intense absorption bands are peaked at 207 and 232 nm; after 275 nm, absorption is not observed. The absorption spectrum of *trans*-$[Pb(DMTU)_4Cl_2]$ particles deposited at the surface of the quartz substrate (Figure 1h) is presented in Figure 2c by the red line. Two peaks are detectable in the spectrum of (**2**) at 246 and 213 nm, and the long-wavelength structureless wing that stretches up to 460 nm is probably formed by the contributions from both scattering and absorption.

The photoluminescence of DMTU was found to be below the detection limit at the excitation both in the main absorption bands in the deep UV and in other wavelengths in the UV within the 220−400 nm range. This absence of luminescence from DMTU is likely due to intersystem crossing that transfers excitation to a long-lived triplet state, and the latter experiencing nonradiative decay. In contrast, the photoluminescence spectra of *trans*-$[Pb(DMTU)_4Cl_2]$ recorded at different excitation wavelengths in the range of 250−450 nm (Figure 2b) demonstrate an intense broad luminescence band in the green peaking approximately at 549 nm with a bandwidth of 110 nm and with no significant dependence of the peak position and the widths on the excitation wavelength. The CIE coordinates (0.374, 0.536), correlated color temperature CCT = 4802.6 K, and color rendering index CRI = 45.17 were calculated from one representative luminescence spectrum at 350 nm excitation (Figure 2e). The excitation spectrum (Figure 2a) of this luminescence demonstrates nonmonotonic behavior with the prominent growth at a shorter-wavelength boundary of the investigated excitation wavelength range. This behavior is somehow unique both for inorganic phosphors as well as for metal−organic frameworks extensively studied in the past few years.[2−8] The photoluminescence excitation (PLE) spectrum

https://doi.org/10.1021/acsanm.1c00162
ACS Appl. Nano Mater. 2021, 4, 3654−3663

can be concerned as formed by the superposition of several excited states, one at 250 nm being likely to be ascribed to the excited state of DMTU, while lower-lying states are absent in the free DMTU molecule. However, all of these excited states experience relaxation to lower excited states that is the source of a single emission band. This feature distinguishes the *trans*-$[Pb(DMTU)_4Cl_2]$ metal−organic compound from such a Pb-based compound like two-dimensional organic−inorganic hybrid metal halide perovskite $C_8H_{12}N_2PbBr_4$, where the excitation is well interpretable within the interband transition model, while emission is dominated by the decay of self-trapped exciton.[4] However, close similarity can be found in our results with 0D butyl-methyl-piperidinium lead bromide.[7] Based on the analysis of the latter study, we assign the luminescence of *trans*-$[Pb(DMTU)_4Cl_2]$ as formed mainly by the transitions from self-trapped exciton states comprising triplet states $^3P_{0,1,2}$ of Pb^{2+} ions to the ground state singlet $^1S_0$. The excitation spectrum in the range of 2.7−4.5 eV (460−275 nm) is formed mainly by the contribution from allowed $^1S_0-^1P_1$ transition split by the low-symmetry crystal field acting on Pb^{2+} ions with local first coordination sphere symmetry C_{1i} within $PbCl_2S_4$ octahedra. After excitation, the population of $^1P_1$ is evidently efficiently transferred to $^3P_{0,1,2}$ via an intersystem crossing. However, a more intense part of the excitation spectrum above 4.5 eV must be associated with the strong absorption by the organic ligands that is further transferred to Pb^{2+} ions due to spatial proximity of excited molecular orbitals of the DMTU ligand with the Pb^{2+} ion and due to intersystem crossing between the DMTU ligand and the Pb^{2+} ion.

It is well-known that wide enough luminescent bands and PLE dependences owe their broadening to the vibronic nature of corresponding transitions. E.g., the shape of the vibronic luminescent band in the simplest case of a single phonon can be described by the formula

$$I(E_{ph}) \sim \sum_{n=0}^{\infty} \exp(-S)\cdot\frac{S^n}{n!}\cdot \exp\left[-\frac{(E_{ph} - E_{ZPL} + n\cdot\varepsilon_{phonon})^2}{2\sigma^2}\right]\cdot\frac{1}{\exp[\frac{\varepsilon_{phonon}}{k_BT}] - 1}$$

where S is the Huang−Rhys parameter, n is the number of phonons with the energy ε_{phonon}, E_{ZPL} is the energy of the zero-phonon line, and T is the temperature.

The width of these bands is determined by the Huang−Rhys parameter S and the energy of phonon involved in vibronic transition: $\Gamma = 2 \times (2\ln 2 \times S)^{1/2} \times \varepsilon_{phonon} \times \coth(\varepsilon_{phonon}/k_BT)$, where S is the Huang−Rhys parameter, ε_{phonon} is the phonon energy, k_B is the Boltzmann constant, and T is the temperature. The Stokes shift between peaks in the PLE spectrum and the PL spectrum can be estimated via the formula $\Delta_{Stokes} = (2S - 1) \times \varepsilon_{phonon} + \Delta_{ZPL}$, where Δ_{ZPL} is the energy gap between the lowest levels of absorbing and emitting energy states. In the case when S values for absorbing and emitting transitions differ, Δ_{ZPL} must be considered as an effective one since it will include possible correction due to variation of the shapes of these transitions. For the lowest sub-band in the excitation spectrum of *trans*-$[Pb(DMTU)_4Cl_2]$, the value Δ_{Stokes} = 0.79 eV. Numerical analysis shows that for our experimental value of Γ = 0.48 eV and a rather small Stokes shift specified above the Huang−Rhys parameter cannot be higher than 4.77. The corresponding value of ε_{phonon} necessary to satisfy both the observed luminescence bandwidth and Stokes shift is of the order of 90 meV. The modeling of the shape of the *trans*-$[Pb(DMTU)_4Cl_2]$ luminescence spectrum was performed using the multiphonon model assuming a single zero-phonon line and single effective phonon energy, while values of S and ε_{phonon} were fitted in the vicinity of initial values specified above. Satisfactory fit with the 0.6% residual discrepancy was found for the Huang−Rhys parameter value S = 4.25, zero-phonon energy of 2.63 eV, and effective phonon energy of 87 meV. The difference between energies of zero-phonon levels of first absorbing and emitting states corresponding to these values is 0.138 eV. The value of the Huang−Rhys parameter obtained for Pb^{2+} ions in S_4Cl_2 octahedra is much lower than recently found for Sb^{3+} ions in the chlorine environment;[54] nevertheless, the extremely high role of vibronic interaction in the formation of the spectral profile of *trans*-$[Pb(DMTU)_4Cl_2]$ luminescence is retained. A considerable difference between S values in two cases must be ascribed to the specific environment of the Pb^{2+} ion in *trans*-$[Pb(DMTU)_4Cl_2]$ that is featured by a large difference of electronegativity of two different kinds of atoms forming the local environment of the former.

The decay curve of the photoluminescence of *trans*-$[Pb(DMTU)_4Cl_2]$ (Figures 2d, S5, and Table S3) shows mainly biexponential behavior with the fast decay time of 0.02 ms and long decay time of the order of 4 ms. A number of compounds with organic ligand-originating luminescence exhibit decay times in the nanosecond temporal range. Alternatively, some organic−inorganic hybrid metal halides exist with extremely large ligand luminescence decay times up to 0.47 s.[55] When luminescence of rare-earth-based or transition-metal-doped materials occurs through the metal ion luminescing center, then decay times are determined by the lifetime of the lowest excited state of the metal ion and can lie in the millisecond range like in the case of the Mn^{2+} doping ion. In our case, the observed fast decay time of 0.02 ms admits that luminescence of *trans*-$[Pb(DMTU)_4Cl_2]$ is not due to the organic ligand, and one can suggest that this fast decay time is the lifetime of the main luminescing center Pb^{2+}. At the same time, one more state exists with a radiative lifetime of the order of several milliseconds. This state must be ascribed to $^3P_0$, which is weakly luminescing due to the doubly forbidden nature of the $^3P_0-^1S_0$ transition. However, $^3P_0$ thermally transfers its population to the $^3P_1$ state that lumineses with a lifetime of 0.02 ms at room temperature. One may note that the luminescence lifetime in *trans*-$[Pb(DMTU)_4Cl_2]$ (20 ms) is considerably larger than the lifetime in such an efficient 0D hybrid halide phosphor like $Bmpip_2PbBr_4$ (66 ns) and slightly larger than the lifetime for similar complexes with another s^2 ion, Ge^{2+}, and Sn^{2+} (4 and 2.6 ms, correspondingly).[7] The preserving of high PLQY found for *trans*-$[Pb(DMTU)_4Cl_2]$ means that nonradiative losses characteristic for *trans*-$[Pb(DMTU)_4Cl_2]$ are considerably weaker than, e.g., in materials based on piperidinium.

The sample showed PLQY equal to 91, 85, and 79% under 365, 385, and 405 nm excitation, respectively (Figure 2f). Due to the possible involvement of interaction between vibronic systems of the organic ligand and of the metal ion, the PLQY may be dependent on the excitation wavelength, in contrast to some organic dyes that demonstrate uniformity of PLQY on the excitation wavelength. The maximum PLQY = 91% is measured in the region of direct excitation of Pb^{2+} singlet−singlet transition within the $PbCl_2S_4$ complex. i.e., in the vicinity of 365 nm (Figure 2f). High PLQY indicates that the concentration quenching of the luminescence in the system of Pb(II) ions is practically absent at the characteristic distance of

https://doi.org/10.1021/acsanm.1c00162
ACS Appl. Nano Mater. 2021, 4, 3654−3663

9.4 Å. Another well-known condition for achieving high PLQY is the absence of intersystem crossing transitions, which usually promote the population of extremely long-living triplet states originating from the organic ligand. The addition of heavy ions with a high spin−orbit coupling constant often stimulates intersystem crossing transitions and decreases PLQY that is commonly referred to as a heavy-ion effect. The lead ion is featured by a high spin−orbit coupling constant of the order of 7000 cm^{-1}. Therefore, we deduce that in our material, the heavy-ion effect is not pronounced that promotes achieving high PLQY.

The remote phosphor light source based on the *trans*-$[Pb(DMTU)_4Cl_2]$ compound showed remarkable stability under continuous pumping in the ambient conditions (Figure 3). After 1 day of continuous irradiation at 405 nm, no signs of its photodegradation were detected (Figure S6). The ratio $I_{450-750}/I_{370-450}$ of the integral intensity of the photoluminescence spectrum in the range of 450−750 nm ($I_{450-750}$) to the integral intensity in the range of 370−450 nm ($I_{370-450}$) of excitation blue light changed from 92 to 88% after 24 h, i.e., less than 5% change (Figure S7). The spectrum of a remote phosphor lamp constructed of 405 nm LED with a total electrical power of 12 W and the *trans*-$[Pb(DMTU)_4Cl_2]$ layer positioned at 1 cm from the LED showed two maxima (405 and 550 nm) (Figure S6), resulting in near-white light emission with CIE coordinates (0.309, 0.391), color rendering index CRI = 58.8, and correlated color temperature CCT = 6370 K (Figure 3). Thermal stability investigation of *trans*-$[Pb(DMTU)_4Cl_2]$ shows that the compound melts without decomposition at 109.6 °C and begins to decompose at 195.9 °C (Figure S8).

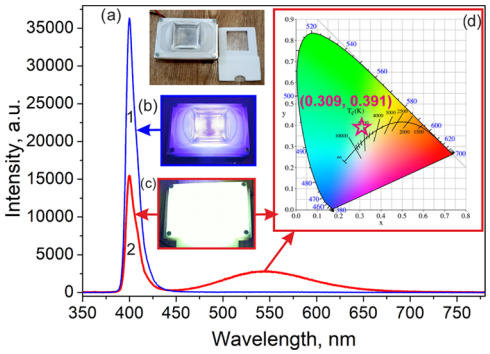

Figure 3. Lamp with remote construction and color characteristics. The lamp with remote construction (a) uses four 3 W LEDs (b) with spectrum maxima at 405 nm (1). The phosphor remote lamp using *trans*-$[Pb(DMTU)_4Cl_2]$ (c) shows the spectrum with two maxima (405 and 550 nm) (2) resulting in near-white light emission with CIE coordinates (0.309, 0.391) (d), color rendering index CRI = 58.8 and correlated color temperature CCT = 6370 K.

Time Dependent-Density Functional Theory (TD-DFT) Simulation of DMTU and *trans*-$[Pb(DMTU)_4Cl_2]$. TD-DFT calculations of the DMTU molecule require the introduction of five different transitions, two of them being nearly degenerate, to describe the absorption spectra in the 200−300 nm range (Figure 4a, see for details Figure S9 and Table S4). The wavelength of S_0-S_1 electronic excitation, which corresponds to the HOMO−LUMO electron transition, is 289 nm in a vacuum and is blue-shifted to approximately 270 nm in water. The oscillator strength of S_0-S_1 excitation is very small (see Figure S9). The most prominent transitions, according to calculation, denoted as $S_0-S_{1,2,3,4}$, belong to the 200−290 nm range. The

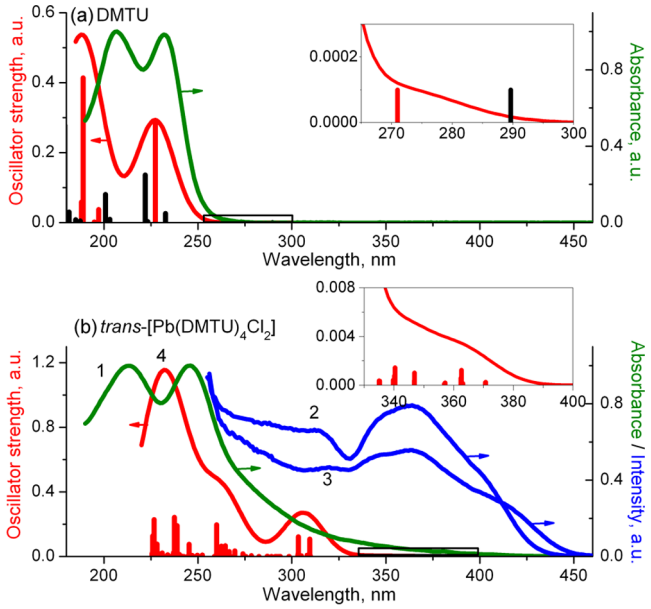

Figure 4. Experimental and calculated absorption spectra for DMTU and *trans*-$[Pb(DMTU)_4Cl_2]$. (a) Experimental absorption (green curve) and TD-DFT calculated absorption spectra in water (red curve and red bars) for DMTU. Black bars for DMTU are given in a vacuum. Inset: calculated absorption of DMTU in the vicinity of S_0. (b) Experimental absorption (1), experimental excitation (2,3), and TD-DFT absorption (4) spectra of *trans*-$[Pb(DMTU)_4Cl_2]$: 1, 2, particles deposited at the surface of quartz substrate; 3, powder; and 4, vacuum. TD-DFT absorption transitions are shown in the graph (red lines). Excitation spectra were measured at λ_{em} = 550 nm. Inset: calculated absorption of *trans*-$[Pb(DMTU)_4Cl_2]$ in the vicinity of HOMO−LUMO transition.

molecular orbitals that contribute to these transitions are from HOMO − 1 to LUMO + 2, and are shown in Figure S10. In TD-DFT spectra, no low-energy electronic states were found, which correspond to the absorption wavelengths above 290 nm, in an excellent agreement with the experiment (Figure 4a).

Simulation of TD-DFT spectra of the $(DMTU)_8PbCl_2$ cluster is computationally complex due to a very large electronic system. To cover the same spectral range, 150 electronic states were used in the calculation. The computed absorption spectrum of $(DMTU)_8PbCl_2$ is presented in Figure 4b as a red line.

A prominent feature of the calculated spectrum is the prediction of the appearance of the absorption well above the limit characteristic for pure DMTU, i.e., above 290 nm, in qualitative agreement with the experiment. The characteristic energy of transition between HOMO and LUMO equals to 3.4 eV that is noticeably lower than the absorption range of DMTU (4.28 eV, or, to be more realistic, above 5.3 eV) in qualitative agreement with the excitation spectrum of *trans*-$[Pb(DMTU)_4Cl_2]$ (Figure 4b). The lowest-energy electronic excitation at 363 nm is dominated by the HOMO−LUMO transition of the complex. The contributions for the high-energy excitations are presented in Figure S11 and Table S4. According to the calculation, HOMO and HOMO-1 orbitals are composed of 3p orbitals of the chlorine ion, while LUMO and LUMO+1 are mainly contributed by 6p orbitals of the lead ion. Therefore, the transition enabling long-wavelength excitation is supposedly the one corresponding to the electron transfer from the chlorine ion orbitals to the excited state of the Pb^{2+} ion. TD-DFT calculations indicate a rather unique scheme of the formation of a sequence of absorption bands, namely, due to the transitions

https://doi.org/10.1021/acsanm.1c00162
ACS Appl. Nano Mater. 2021, 4, 3654−3663

from a variety of lower occupied orbitals to the same unoccupied ones.

CONCLUSIONS

A metal−organic compound, *trans*-[Pb(DMTU-S)$_4$Cl$_2$], with a heterogeneous local environment of the Pb^{2+} ion, was synthesized. XRD analysis identified this new material as belonging to the class of 0D metal−organic nanostructure frameworks. The compound is featured by a wide luminescent band peaking at 549 nm with 110 nm width, by the wide excitation band from 450 nm down to 260 nm at least, by 20 microsecond lifetime, and by high quantum yield achieving 91% at 365 nm. Luminescence is assigned to Pb^{2+} ions within S_4Cl_2 octahedra, and its lineshape is described by the vibronic model with the Huang−Rhys parameter $S = 4.25$ and effective phonon energy of the order of 90 meV. The excitation spectrum is formed by the contributions from direct excitation of Pb^{2+} ions and by energy transfer from the orbitals originating from organic ligands that were modified after the formation of the *trans*-[Pb(DMTU-S)$_4$Cl$_2$]-nanostructured complex. No considerable influence of concentration quenching in the system of Pb^{2+} ions is detected at a characteristic distance of 9.4 Å. The new compound is featured by low-energy consumption upon production in comparison with inorganic materials and high-performance stability comparable with the latter, which is promising for a number of applications in photonics.

ASSOCIATED CONTENT

Supporting Information

The Supporting Information is available free of charge at https://pubs.acs.org/doi/10.1021/acsanm.1c00162.

Difference X-ray powder patterns of *trans*-[Pb(DMTU)-4Cl2] obtained by kneading and crystallization from an aqueous solution (Figure S1); main geometric parameters (Å, °) of (1) and (2) (Table S1); *trans*-[Pb(DMTU-S)4Cl2] crystal structure with 30 irreducible atoms in the conventional cell optimized in P21/c symmetry via the CRYSTAL17 code with the B3LYP functional and basis sets (Figure S2); model of the Pb(DMTU)$_8$Cl$_2$ cluster for absorption spectra simulation (Figure S3); hydrogen-bond geometry in (1) and (2) structures (Å, °) (Table S2); hydrogen-bond pattern of DMTU and *trans*-[Pb(DMTU)$_4$Cl$_2$] (F) (Figure S4); fitting of *trans*-[Pb(DMTU)$_4$Cl$_2$] photoluminescence decay (Figure S5); parameters of PL decay of *trans*-[Pb(DMTU)$_4$Cl$_2$] (Table S3); time-dependent change of the spectrum of the remote phosphor light source based on the *trans*-[Pb(DMTU)$_4$Cl$_2$] compound and 405 nm LED with a total electrical power of 12 W (Figure S6); time dependent ratio I450-750/I370-450 of integral intensity of photoluminescence spectrum (Figure S7); TG/DSC curves of *trans*-[Pb(DMTU)$_4$Cl$_2$] (Figure S8); calculated absorption spectrum of DMTU in gas phase (Figure S9); TD-DFT absorption transitions* of *trans*-[Pb-(DMTU)$_4$Cl$_2$](DMTU)$_4$ (Table S4); molecular orbitals of DMTU at B3LYP/def2-SVP level of theory (Figure S10); and calculated absorption spectrum of *trans*-[Pb(DMTU)$_4$Cl$_2$] in gas phase (Figure S11) (PDF)

Crystal structure of DMTU (CIF)

Crystal structure of PbCl$_2$(DMTU)$_4$ (CIF)

AUTHOR INFORMATION

Corresponding Authors

Nicolay N. Golovnev − *Siberian Federal University, Krasnoyarsk 660041, Russia*; Email: ngolovnev@sfu-kras.ru

Aleksandr S. Aleksandrovsky − *Siberian Federal University, Krasnoyarsk 660041, Russia; Laboratory of Crystal Physics, Kirensky Institute of Physics, Federal Research Center KSC SB RAS, Krasnoyarsk 660036, Russia;* orcid.org/0000-0003-1821-6718; Email: aleksandrovsky@kirensky.ru

Maxim S. Molokeev − *Siberian Federal University, Krasnoyarsk 660041, Russia; Laboratory of Crystal Physics, Kirensky Institute of Physics, Federal Research Center KSC SB RAS, Krasnoyarsk 660036, Russia; Research and Development Department, Kemerovo State University, Kemerovo 650000, Russia;* orcid.org/0000-0002-8297-0945; Email: msmolokeev@mail.ru

Authors

Marina A. Gerasimova − *Siberian Federal University, Krasnoyarsk 660041, Russia;* orcid.org/0000-0001-8445-2714

Felix N. Tomilin − *Siberian Federal University, Krasnoyarsk 660041, Russia; Laboratory of Crystal Physics, Kirensky Institute of Physics, Federal Research Center KSC SB RAS, Krasnoyarsk 660036, Russia*

Vladimir A. Mironov − *Department of Chemistry, Lomonosov Moscow State University, Moscow 119991, Russia;* orcid.org/0000-0002-9454-5823

Anastasia V. Demina − *Siberian Federal University, Krasnoyarsk 660041, Russia*

Zhiguo Xia − *The State Key Laboratory of Luminescent Materials and Devices, Guangdong Provincial Key Laboratory of Fiber Laser Materials and Applied Techniques, School of Materials Science and Technology, South China University of Technology, Guangzhou 510641, China;* orcid.org/0000-0002-9670-3223

Complete contact information is available at: https://pubs.acs.org/10.1021/acsanm.1c00162

Notes

The authors declare no competing financial interest.

ACKNOWLEDGMENTS

This work is supported by the RFBR according to the research project No. 19-52-80003. This work is also supported by the National Natural Science Foundation of China (51961145101). V.M. thanks Russian Foundation for Basic Research (project number 19-03-00043) for funding. The use of equipment of Krasnoyarsk Regional Center of Research Equipment of Federal Research Center "Krasnoyarsk Science Center SB RAS" is acknowledged. The authors thank JSCC RAS for providing computational resources.

REFERENCES

(1) Allendorf, M. D.; Bauer, C. A.; Bhakta, R. K.; Houk, R. J. T. Luminescent metal−organic frameworks. *Chem. Soc. Rev.* **2009**, *38*, 1330−1352.

(2) Benin, B. M.; Dirin, D. N.; Morad, V.; Worle, M.; Yakunin, S.; Raino, G.; Nazarenko, O.; Fischer, M.; Infante, I.; Kovalenko, M. V. Highly Emissive Self-Trapped Excitons in Fully Inorganic Zero-Dimensional Tin Halides. *Angew. Chem., Int. Ed.* **2018**, *57*, 11329−11333.

(3) Zhou, C.; Lin, H. R.; Tian, Y.; Yuan, Z.; Clark, R.; Chen, B. H.; van de Burgt, L. J.; Wang, J. C.; Zhou, Y.; Hanson, K.; Meisner, Q. J.; Neu, J.; Besara, T.; Siegrist, T.; Lambers, E.; Djurovich, P.; Ma, B. W. Luminescent zero-dimensional organic metal halide hybrids with near-unity quantum efficiency. *Chem. Sci.* **2018**, *9*, 586−593.
(4) Lin, H.; Zhou, C. K.; Chaaban, M.; Xu, L. J.; Zhou, Y.; Neu, J.; Worku, M.; Berkwits, E.; He, Q.; Lee, S.; Lin, X. S.; Siegrist, T.; Du, M. H.; Ma, B. W. Bulk assembly of zero-dimensional organic lead bromide hybrid with efficient blue emission. *ACS Mater. Lett.* **2019**, *1*, 594−598.
(5) Zhou, J.; Li, M. Z.; Ning, L. X.; Zhang, R. L.; Molokeev, M. S.; Zhao, J.; Yang, S. Q.; Han, K. L.; Xia, Z. G. Broad-Band Emission in a Zero-Dimensional Hybrid Organic [$PbBr_6$] Trimer with Intrinsic Vacancies. *J. Phys. Chem. Lett.* **2019**, *10*, 1337−1341.
(6) Mohammed, O. F. Outstanding challenges of zero-dimensional perovskite materials. *J. Phys. Chem. Lett.* **2019**, *10*, 5886−5888.
(7) Morad, V.; Shynkarenko, Y.; Yakunin, S.; Brumberg, A.; Schaller, R. D.; Kovalenko, M. V. Disphenoidal Zero-Dimensional Lead, Tin, and Germanium Halides: Highly Emissive Singlet and Triplet Self-Trapped Excitons and X-ray Scintillation. *J. Am. Chem. Soc.* **2019**, *141*, 9764−9768.
(8) Lin, H.; Zhou, C.; Tian, Y.; Siegrist, T.; Ma, B. Low-dimensional organometal halide perovskites. *ACS Energy Lett.* **2018**, *3*, 54−62.
(9) Singhal, N.; Chakraborty, R.; Ghosh, P.; Nag, A. Low-bandgap $Cs_4CuSb_2Cl_{12}$ layered double perovskite: Synthesis, reversible thermal changes, and magnetic interaction. *Chem. - Asian J.* **2018**, *13*, 2085−2092.
(10) Han, P.; Luo, C.; Yang, S.; Yang, Y.; Deng, W.; Han, K. All-Inorganic Lead-Free 0D Perovskites by a Doping Strategy to Achieve a PLQY Boost from<2% to 90%. *Angew. Chem., Int. Ed.* **2020**, *59*, 12709−12713.
(11) McCall, K. M.; Morad, V.; Benin, B. M.; Kovalenko, M. V. Efficient Lone-Pair-Driven Luminescence: Structure−Property Relationships in Emissive $5s^2$ Metal Halides. *ACS Mater. Lett.* **2020**, *2*, 1218−1232.
(12) Arfin, H.; Kshirsagar, A. S.; Kaur, J.; Mondal, B.; Xia, Z.; Chakraborty, S.; Nag, A. (2020). ns^2 Electron (Bi^{3+} and Sb^{3+}) Doping in Lead-Free Metal Halide Perovskite Derivatives. *Chem. Mater.* **2020**, *32*, 10255−10267.
(13) Su, B. B.; Song, G. M.; Molokeev, M. S.; Lin, Z. S.; Xia, Z. G. Synthesis, Crystal Structure and Green Luminescence in Zero-Dimensional Tin Halide $(C_8H_{14}N_2)_2SnBr_6$. *Inorg. Chem.* **2020**, *59*, 9962−9968.
(14) Mao, L.; Guo, P.; Wang, S.; Cheetham, A. K.; Seshadri, R. Design Principles for Enhancing Photoluminescence Quantum Yield in Hybrid Manganese Bromides. *J. Am. Chem. Soc.* **2020**, *142*, 13582−13589.
(15) Zhou, G.; Liu, Z.; Huang, J.; Molokeev, M. S.; Xiao, Z.; Ma, C.; Xia, Z. Unraveling the Near-Unity Narrow-Band Green Emission in Zero-Dimensional Mn^{2+}-Based Metal Halides: A Case Study of $(C_{10}H_{16}N)_2Zn_{1-x}Mn_xBr_4$ Solid Solutions. *J. Phys. Chem. Lett.* **2020**, *11*, 5956−5962.
(16) Ahmad, S.; Saleem, M.; Georgieva, I.; Ruffer, T.; Schaarschmidt, D.; Lang, H.; Murtaza, G.; Hussain, I.; Habib-ur-Rehman, A. A. I.; Malik, M. R.; Ali, S. Synthesis, characterization, DFT calculations and antimicrobial studies of cadmium (II) sulfate complexes of thioureas and 2-mercaptopyridine; X-ray structures of polymeric diaqua (N, N′-dimethylthiourea) sulfatocadmium (II) and bis (2-mercaptopyridine) sulfatocadmium (II). *Polyhedron* **2018**, *149*, 126−133.
(17) Seerat-ur-Rehman; Ahmad, S.; Choudhary, M. A.; Tahir, M. N.; Ali, I.; Aslam, M.; Fettouhi, M.; Isab, A. A.; Alotaibi, M. A.; Alharthi, A. I. Synthesis, X-ray structures and antibacterial activities of silver (I) complexes of 1, 3-bis (diphenylphosphano) propane (Dppp) and N, N′-dimethylthiourea (Dmtu). *Polyhedron* **2020**, *175*, No. 114209.
(18) de Souza, R. F. F.; Cunha, G. A.; Pereira, J. C. M.; Garcia, D. M.; Bincoletto, C.; Goto, R. N.; Leopoldino, A. M.; Silva, I. C.; Pavan, F. R.; Deflon, V. M.; Almeida, E. T.; Mauro, A. E.; Netto, A. V. G. Orthopalladated acetophenone oxime compounds bearing thioamides as ligands: Synthesis, structure and cytotoxic evaluation. *Inorg. Chim. Acta* **2019**, *486*, 617−624.
(19) Ozturk, I. I.; Yarar, S.; Banti, C. N.; Kourkoumelis, N.; Chrysouli, M. P.; Manoli, M.; Tasiopoulos, A. J.; Hadjikakou, S. K. QSAR studies on antimony (III) halide complexes with N-substituted thiourea derivatives. *Polyhedron* **2017**, *123*, 152−161.
(20) Marverti, G.; Cusumano, M.; Ligabue, A.; Di Pietro, M. L.; Vainiglia, P. A.; Ferrari, A.; Bergomi, M.; Moruzzi, M. S.; Frassineti, C. Studies on the anti-proliferative effects of novel DNA-intercalating bipyridyl−thiourea−Pt (II) complexes against cisplatin-sensitive and-resistant human ovarian cancer cells. *J. Inorg. Biochem.* **2008**, *102*, 699−712.
(21) Mamaeva, E. A.; Bakibaev, A. A. Oxidative azacyclization of 1-monosubstituted thioureas in reaction with [bis (acyloxy) iodo] arenes to form 1, 2, 4-thiadiazole derivatives. *Tetrahedron* **2003**, *59*, 7521−7525.
(22) Sulaiman, A.; Kalia, N.; Bhatia, G.; Kaur, M.; Fettouhi, M.; Altaf, M.; Baig, N.; Kawde, A.; Isab, A. Cytotoxic effects of gold(I) complexes against colon, cervical and osteo carcinoma cell lines: a mechanistic approach. *New J. Chem.* **2019**, *43*, 14565−14574.
(23) Aziz, I.; Sirajuddinb, M.; Munira, A.; Tirmizia, S. A.; Nadeema, S.; Tahird, M. N.; Sajjade, W. Synthesis, Characterization, DNA Interaction Study, Antibacterial and Anticancer Activities of New Palladium(II) Phosphine Complexes. *Russ. J. Gen. Chem.* **2018**, *88*, 551−559.
(24) Han, A.; Ozturk, I. I.; Banti, C. N.; Kourkoumelis, N.; Manoli, M.; Tasiopoulos, A. J.; Owczarzak, A. M.; Kubicki, M.; Hadjikakou, S. K. Antimony (III) halide compounds of thioureas: Structures and biological activity. *Polyhedron* **2014**, *79*, 151−160.
(25) Sigman, M. S.; Jacobsen, E. N. Schiff Base Catalysts for the Asymmetric Strecker Reaction Identified and Optimized from Parallel Synthetic Libraries. *J. Am. Chem. Soc.* **1998**, *120*, 4901−4902.
(26) Golovnev, N. N.; Molokeev, M. S.; Sterkhova, I. V.; Lesnikov, M. K. Crystallographic, thermal and spectroscopic characterization of the anhydrous thiourea−barbituric acid and thiourea−2-thiobarbituric acid co-crystals. *J. Mol. Struct.* **2019**, *1176*, 865−870.
(27) Ganesh, V.; Shkira, M.; Yahia, I. S.; Parakkandy, J. M.; AlFaify, S. Phenol red dyed Bis thiourea Zinc acetate crystal growth and characterization for electro-optic applications. *Optik* **2018**, *158*, 997−1005.
(28) Ramteke, S. P.; Anis, M.; Baig, M. I.; Muley, G. G. Influence of Cu2+ ion on structural, luminescence and dielectric properties of zinc thiourea chloride metal-organic complex crystal. *Optik* **2018**, *154*, 275−279.
(29) Anis, M.; Baig, M. I.; Muley, G. G.; AlFaify, S.; Khand, M. A. Impact of increasing concentration of l-alanine environment on structural, UV−vis, SHG efficiency, luminescence and dielectric traits of zinc thiourea chloride (ZTC) crystal. *Optik* **2019**, *185*, 317−324.
(30) Anis, M.; Baig, M. I.; Muley, G. G.; Hussaini, S. S.; Shirsat, M. D. Monocrystal growth, X-ray diffraction, photoluminescence, thermal and dielectric studies of cadmium thiourea acetate complex doped with L-cystine. *Optik* **2016**, *127*, 12043−12047.
(31) Mahendra, K.; D'Souza, A.; Udayashankar, N. K. Effect of Zn doping on the structural, optical, photoluminescence and mechanical properties of thiourea barium chloride (TBC) crystal. *Materials Today Comm.* **2017**, *13*, 178−185.
(32) Azhar, S. M.; Rabbani, G.; Shirsat, M. D.; Hussaini, S. S.; Baig, M. I.; Ghramh, H. A.; Anis, M. Luminescence, laser induced nonlinear optical and surface microscopic studies of potassium thiourea chloride crystal. *Optik* **2018**, *165*, 259−265.
(33) Grifasi, F.; Chierotti, M. R.; Garino, C.; Gobetto, R.; Priola, E.; Diana, E.; Turci, F. Solvent-Free Synthesis of Luminescent Copper(I) Coordination Polymers with Thiourea Derivatives. *Cryst. Growth Des.* **2015**, *15*, 2929−2939.
(34) Cîrcu, V.; Ilie, M.; Ilis, M.; Dumitras, F.; Neagoe, I.; Pasculescu, S. Luminescent cyclometallated platinum(II) complexes with N-benzoyl thiourea derivatives as ancillary ligands. *Polyhedron* **2009**, *28*, 3739−3746.
(35) Małecki, J. G.; Nycz, J. Ruthenium(II) hydridecarbonyl complex with N,N′-bis(2-pyridyl)thiourea as co-ligand. *Polyhedron* **2013**, *55*, 49−56.

https://doi.org/10.1021/acsanm.1c00162
ACS Appl. Nano Mater. 2021, 4, 3654−3663

(36) Iwanaga, M.; Shirai, M.; Tanaka, K.; Hayashi, T. Self-376 Trapped States and Related Luminescence in $PbCl_2$ Crystals. *Phys. Rev. B: Condens. Matter Mater. Phys.* **2002**, *66*, 4304−4312.
(37) Iwanaga, M.; Watanabe, M.; Hayashi, T. Charge separation of excitons and the radiative recombination process in $PbBr_2$ crystals. *Phys. Rev. B: Condens. Matter Mater. Phys.* **2000**, *62*, 10766−10773.
(38) Hefter, G. T. Stability constants for the lead (II)-halide systems. *Polyhedron* **1990**, *9*, 2429−2432.
(39) Fedorov, V. A.; Fedorova, A. V.; Golovnev, N. N.; Nifantieva, G. G. Complexation of bismuth (III) and lead (II) ions with thiourea and its derivatives. *Russ. J. Inorg. Chem.* **1979**, *24*, 146−148.
(40) Sheldrick, G. M. A short history of SHELX. *Acta Crystallogr., Sect. A: Found. Crystallogr.* **2008**, *64*, 112−122.
(41) Spek, A. L. J. Single-crystal structure validation with the program PLATON. *J. Appl. Cryst.* **2003**, *36*, 7−13.
(42) Pennington, W. T. DIAMOND−visual crystal structure information system. *J. Appl. Cryst.* **1999**, *32*, 1028−1029.
(43) *Bruker AXS TOPAS V4: General Profile and Structure Analysis Software For Powder Diffraction Data. User's Manual*; Bruker AXS: Karlsruhe, Germany, 2008.
(44) Dovesi, R.; Erba, A.; Orlando, R.; Zicovich-Wilson, C. M.; Civalleri, B.; Maschio, L.; Rerat, M.; Casassa, S.; Baima, J.; Salustro, S.; Kirtman, B. Quantum-mechanical condensed matter simulations with CRYSTAL17. *Wiley Interdiscip. Rev.: Comput. Mol. Sci.* **2018**, *8*, No. e1360.
(45) Lee, C.; Yang, W.; Parr, R. G. Development of the Colle-Salvetti correlation-energy formula into a functional of the electron density. *Phys. Rev. B* **1988**, *37*, 785−787.
(46) Becke, A. D. Density-functional exchange-energy approximation with correct asymptotic behavior. *Phys Rev A* **1988**, *38*, 3098−3105.
(47) Oliveira, D. V.; Peintinger, M. F.; Laun, J.; Bredow, T. BSSE-correction scheme for consistent gaussian basis sets of double-and triple-zeta valence with polarization quality for solid-state calculations. *J. Comp. Chem.* **2019**, *40*, 2364−2376.
(48) Zagorac, D.; Doll, K.; Schoen, J. C.; Jansen, M. Ab initio structure prediction for lead sulfide at standard and elevated pressures. *Phys. Rev. B* **2011**, *84*, No. 045206.
(49) Metz, B.; Stoll, H.; Dolg, M. Small-core multiconfiguration-Dirac−Hartree−Fock-adjusted pseudopotentials for post-d main group elements: Application to PbH and PbO. *J. Chem. Phys.* **2000**, *113*, 2563−2569.
(50) Dovesi, R.; Saunders, V. R.; Roetti, C.; Orlando, R.; Zicovich-Wilson, C. M.; Pascale, F.; Civalleri, B.; Doll, K.; Harrison, N. M.; Bush, I. J.; D'Arco, P.; Llunell, M.; Causà, M.; Noël, Y.; Maschio, L.; Erba, A.; Rerat, M.; Casassa, S. *CRYSTAL17 User's Manual*; University of Torino: Torino, 2017.
(51) Civalleri, B.; D'Arco, Ph.; Orlando, R.; Saunders, V. R.; Dovesi, R. Hartree−Fock geometry optimisation of periodic systems with the Crystal code. *Chem. Phys. Lett.* **2001**, *348*, 131−138.
(52) Marenich, A. V.; Cramer, C. J.; Truhlar, D. G. Universal solvation model based on solute electron density and on a continuum model of the solvent defined by the bulk dielectric constant and atomic surface tensions. *J. Phys. Chem. B.* **2009**, *113*, 6378−6396.
(53) Baur, W. H. The geometry of polyhedral distortions. Predictive relationships for the phosphate group. *Acta Crystallogr., Sect. B: Struct. Crystallogr. Cryst. Chem.* **1974**, *30*, 1195−1215.
(54) Jing, Y.; Liu, Y.; Jiang, X.; Molokeev, M. S.; Lin, Z.; Xia, Z. Boosting triplet self-trapped exciton emission in Te (IV)-doped Cs_2SnCl_6 perovskite variants. *Chem. Mater.* **2020**, *32*, 5327−5334.
(55) Yang, X.; Yan, D. Long-afterglow metal−organic frameworks: reversible guest-induced phosphorescence tunability. *Chem. Sci.* **2016**, *7*, 4519−4526.

https://doi.org/10.1021/acsanm.1c00162
ACS Appl. Nano Mater. 2021, 4, 3654−3663